PNAS RESEARCH ARTICLE | CHEMISTRY

Driving force and pathway in polyelectrolyte complex coacervation

Shensheng Chen[a] and Zhen-Gang Wang[a,1]

Edited by Matthew Tirrell, The University of Chicago, Chicago, IL; received June 10, 2022; accepted August 1, 2022

There is notable discrepancy between experiments and coarse-grained model studies regarding the thermodynamic driving force in polyelectrolyte complex coacervation: experiments find the free energy change to be dominated by entropy, while simulations using coarse-grained models with implicit solvent usually report a large, even dominant energetic contribution in systems with weak to intermediate electrostatic strength. Here, using coarse-grained, implicit-solvent molecular dynamics simulation combined with thermodynamic analysis, we study the potential of mean force (PMF) in the two key stages on the coacervation pathway for symmetric polyelectrolyte mixtures: polycation–polyanion complexation and polyion pair–pair condensation. We show that the temperature dependence in the dielectric constant of water gives rise to a substantial entropic contribution in the electrostatic interaction. By accounting for this electrostatic entropy, which is due to solvent reorganization, we find that under common conditions (monovalent ions, room temperature) for aqueous systems, both stages are strongly entropy-driven with negligible or even unfavorable energetic contributions, consistent with experimental results. Furthermore, for weak to intermediate electrostatic strengths, this electrostatic entropy, rather than the counterion-release entropy, is the primary entropy contribution. From the calculated PMF, we find that the supernatant phase consists predominantly of polyion pairs with vanishingly small concentration of bare polyelectrolytes, and we provide an estimate of the spinodal of the supernatant phase. Finally, we show that prior to contact, two neutral polyion pairs weakly attract each other by mutually induced polarization, providing the initial driving force for the fusion of the pairs.

polyelectrolyte complex coacervation | entropy | thermodynamic driving force | coarse-grained simulation | polarization

Significance

Coarse-grained theory and simulation using continuum electrostatics models with implicit solvent are powerful methods for studying electrolyte/polyelectrolyte solutions. Information about the solvent degrees of freedom becomes hidden in the coarse-grained representation, which can lead to inconsistencies in interpreting experimental data if this information is not properly accounted for. Here we show that the temperature dependence in the dielectric constant of water can be exploited to extract the solvent entropy contribution in the electrostatic interactions, thereby resolving a major discrepancy between experiments and coarse-grained model studies concerning the thermodynamic driving force (i.e., entropy vs. energy) for polyelectrolyte complex coacervation. For weakly charged systems, this electrostatic entropy constitutes the main contribution to the overall entropy change.

Polyelectrolyte (PE) complex coacervation refers to an associative liquid–liquid phase separation (LLPS) upon mixing oppositely charged polyelectrolyte solutions, which results in the formation of a coacervate phase containing most of the polyions and a dilute supernatant phase (1, 2). This electrostatically induced LLPS underpins a number of important biological phenomena such as membraneless organelles in cells (3–6) and ocean life adhesion (7–11) and is also being exploited in novel biomedical and biomimetic applications such as drug delivery (12–14) and underwater adhesion (10, 15–19). In the 6 decades since the pioneering theoretical work by Overbeek and Voorn (20), significant progress has been made on both the theory/simulation and experiment fronts in understanding the many effects on this LLPS, such as chain connectivity (21–30), excluded volume (22, 25, 31–35), charge sequence (36–40), ion pairing (22, 41, 42), charge asymmetry (43–47), temperature (48–53), pH (54–57), and solvent quality (58–60). We refer readers to several excellent recent reviews (61–65). Despite these advances, however, some fundamental questions remain in regard to the thermodynamic driving force and the mechanism for coacervation.

There has been a notable discrepancy between experimental results and simulation studies concerning the thermodynamic driving force. Thermodynamically, polyelectrolyte complex coacervation can be considered a two-stage process: first, the complexation of polycations and polyanions into polyion pairs, and second, the condensation of the polyion pairs into the coacervate phase (66–71), with the first stage dominating the free energy change for the overall process. Based on isothermal titration calorimetry (72), Tirrell and coworkers determined the thermodynamic driving forces for both stages and found that for each stage the free energy change is dominated by entropy with negligible enthalpic contribution (71, 73). The entropy dominance was also demonstrated by Schlenoff and coworkers in complex coacervation for some common polyelectrolytes (74, 75). On the other hand, coarse-grained computer simulation studies of the complexation of two oppositely charged polyelectrolyte generally found substantial energy contribution in the free energy change (76–80). In a seminal work, Ou and Muthukumar (76), using

Author affiliations: [a]Division of Chemistry and Chemical Engineering, California Institute of Technology, Pasadena, CA 91125

Author contributions: S.C. and Z.-G.W. designed research, performed research, analyzed data, and wrote the paper.

The authors declare no competing interest.

This article is a PNAS Direct Submission.

[1]To whom correspondence may be addressed. Email: zgw@caltech.edu.

This article contains supporting information online at https://www.pnas.org/lookup/suppl/doi:10.1073/pnas.2209975119/-/DCSupplemental.

Published August 29, 2022.

Langevin dynamics simulation, found that the process is energy driven for electrostatic strength $\xi = l_B/l < 1.5$, where l_B is the Bjerrum length and l is the spacing between charges along the chain backbone. The electrostatic energy contribution remains favorable up to $\xi = 2.5$. Similar results were reported in simulations from Rathee et al. (78) and from Singh and Yethiraj (79). The discrepancy becomes especially obvious in the range of $\xi < 2$ for which simulations predicted significantly favorable energetic contributions, while experiments found the energetic contribution to be generally small and unfavorable (75, 81). Furthermore, in the relevant range of ξ values ($1 < \xi < 3$) for typical polyelectrolyte complex coacervation systems used in experiments, the enthalpy change, while remaining relatively small, changes sign from positive to negative with increasing ξ (75, 81); this trend is opposite to that observed in the simulation of ref. 76. Because of these differences, Schlenoff and coworkers (74, 75, 82) raised serious concerns about the use of continuum electrostatics to describe polyelectrolyte complex coacervation systems that most simulations (and theories) rely on. This discrepancy between experimental data and simulation results must be resolved in order to continue using coarse-grained simulation/theory with confidence to study the properties of polyelectrolyte complex coacervation.

The large entropic driving force in polyelectrolyte complex coacervation observed in experiments is commonly believed to arise from the counterion release upon complexation between oppositely charged polyelectrolyte chains (61–63, 76, 83). However, this counterion-release mechanism can only explain the entropy dominance in the regime of strong electrostatic interactions ($\xi > 2.5$), in which over 60% of the counterions are bound to the uncomplexed polyions (76). As the electrostatic strength decreases, the counterion-release entropy becomes less important and is only a minor contribution to the overall free energy change when $\xi < 1.5$. Thus, there is a missing entropy contribution that is not accounted for in the coarse-grained simulations. In this article, we will show that this missing entropy is rooted in the electrostatic interaction used in the coarse-grained models.

To appreciate the role of entropy in electrostatics, we note that in implicit solvent models with dielectric continuum treatment of electrostatics, the interaction energy between two charges q_i and q_j, separated by distance r_{ij} in a solvent of electric permittivity ϵ, $E_{el} = \sum_{i,j} \frac{q_i q_j}{4\pi\epsilon r_{ij}}$, is in fact a potential of mean force (PMF) with the solvent degrees of freedom averaged out. The dielectric constant of water (the primary solvent used in coacervation studies) is known to have significant temperature dependence (84). The temperature-dependent dielectric constant has been shown to be a major factor (50, 53) responsible for the lower critical solution temperature behavior in some polyelectrolyte complex coacervation systems (82, 85, 86). More importantly, the temperature dependence of dielectric constant means the electrostatic energy, E_{el}, has an entropic contribution (87, 88). By interpreting E_{el} as a pure energy term in the thermodynamic analysis of polyelectrolytes, previous works did not consider the entropic contribution in this electrostatic energy. In this work, we show that by properly accounting for the entropic contribution in E_{el} from the coarse-grained molecular dynamics simulation, both stages of the polyelectrolyte complex coacervation are found to be entropy driven with only minor contributions from energy, consistent with known experimental results. Based on the free energy calculation, we analyze the state of the dilute phase and investigate the pathway of pair–pair condensation, which is a key step in the pathway of the second stage in the coacervation.

We start with the free energy F for the canonical system, which is given in terms of the partition function Z as

$$F = -k_B T \ln(Z) = -k_B T \ln\left(\sum_{\Gamma} e^{-E[\Gamma]/k_B T}\right), \quad [1]$$

where k_B, T, and $E[\Gamma]$ are the Boltzmann constant, temperature, and energy for microstate Γ, respectively. In a fully microscopic model, the microstate Γ includes all degrees of freedom, and the energy $E[\Gamma]$ is the true energy, independent of temperature. However, in a coarse-grained model, such as implicit solvent models commonly employed for studying electrolyte and polyelectrolyte systems, Γ refers only to the reduced degrees of freedom, and $E[\Gamma]$ should be interpreted as a PMF, which is generally temperature dependent. Regardless of the degree of coarse graining, the thermodynamic entropy S is given by

$$\begin{aligned} -S = \frac{\partial F}{\partial T} &= -k_B \ln(Z) - k_B T \frac{\partial \ln(Z)}{\partial T} \\ &= \frac{F}{T} - \frac{k_B T}{Z} \sum_{\Gamma} e^{-E[\Gamma]/k_B T} \cdot \left(\frac{E[\Gamma]}{k_B T^2} - \frac{1}{k_B T}\frac{\partial E[\Gamma]}{\partial T}\right) \\ &= \frac{F}{T} - \frac{\langle E \rangle}{T} + \left\langle \frac{\partial E}{\partial T} \right\rangle, \end{aligned} \quad [2]$$

i.e.,

$$-TS = F - \langle E \rangle + T \left\langle \frac{\partial E}{\partial T} \right\rangle. \quad [3]$$

Thus, for a fully microscopic model, the last term is zero, and we recover the well-known relation $-TS = F - \langle E \rangle$. However, for coarse-grained models, the last term is generally nonzero and therefore must be included in the calculation of the true, physical entropy. For implicit-solvent models of electrolyte and polyelectrolyte systems, the temperature dependence of the energy is in the electrostatic interaction E_{el} through the dielectric constant. The nonelectrostatic part of the interaction contributes little to the free energy change in this study, as shown in *SI Appendix*, Fig. S1. For the electrostatic part,

$$\begin{aligned} \left\langle \frac{\partial E_{el}}{\partial T} \right\rangle &= \left\langle \frac{\partial \sum_{i,j} \frac{q_i q_j}{4\pi\epsilon r_{ij}}}{\partial T} \right\rangle \\ &= \left\langle \sum_{i,j} \frac{q_i q_j}{4\pi r_{ij}} \right\rangle \cdot \left(\frac{-1}{\epsilon^2}\right) \cdot \frac{\partial \epsilon}{\partial T} \\ &= -\frac{1}{\epsilon} \cdot \frac{\partial \epsilon}{\partial T} \cdot \langle E_{el} \rangle. \end{aligned} \quad [4]$$

Substituting Eq. **4** into the last term of Eq. **3** yields

$$-TS = F - \langle E \rangle - \langle E_{el} \rangle \cdot \frac{T}{\epsilon} \cdot \frac{\partial \epsilon}{\partial T}. \quad [5]$$

Thus, when there is significant temperature dependence in the dielectric constant, such as in the case of water, the last term in Eq. **5** results in a substantial correction to the calculation of the entropy and energy. We shall call this term the "electrostatic entropy" (after dividing by the temperature), to indicate that this is the entropy contained in the electrostatic interaction potential used in coarse-grained model. The physical origin of this electrostatic entropy is the reorganization of the solvent, particularly in the orientation degrees of freedom of the dipolar solvent molecules. In the Onsager theory for dielectric constant of liquids, the temperature dependence is directly due to the orientation of the

permanent dipoles (89). Although in real liquids such as water, local structural correlations (such as due to hydrogen bonding) result in modification of the dipolar contribution to the dielectric constant (87, 90) and thus more complicated temperature dependence than predicted by the Onsager theory, the dipolar orientation remains the major root cause for the temperature dependence of the dielectric constant. In *SI Appendix*, we provide a simple explanation of the physical basis of the electrostatic entropy based on the dipolar orientation of the solvent molecules.

Using the empirical temperature dependence of the dielectric constant of water given by Malmberg and Maryott (84),

$$\epsilon/\epsilon_0 = 87.74 - 0.4008t + 9.398 \cdot 10^{-4}t^2 - 1.410 \cdot 10^{-6}t^3, \quad [6]$$

where $t = T - 273.15$ and ϵ_0 is the vacuum electric permittivity, we find, at room temperature 298.15 K, $(T/\epsilon)(\partial\epsilon/\partial T) = -1.3576$, and so

$$TS = -F + \langle E\rangle - 1.3576\langle E_{el}\rangle. \quad [7]$$

Since our interest in the thermodynamic analysis involves only changes of thermodynamic functions between different states under isothermal conditions, the more relevant equation is

$$T\Delta S = -\Delta F + \Delta\langle E\rangle - 1.3576\Delta\langle E_{el}\rangle. \quad [8]$$

We note that this equation is unaffected whether or not the self-energy of the ions is included in E_{el} since the self-energies of the ions between the different thermodynamic states are unchanged and will cancel out in taking the difference. From Eq. **8**, we also see that the true energy change ΔU should be $\Delta U = \Delta\langle E\rangle - 1.3576\Delta\langle E_{el}\rangle$. Thus, by properly accounting for the entropic contribution in the electrostatic interaction, both the entropic and energetic contributions in driving force will be altered. For comparison in our later discussion, we will use the notation $\Delta U^\dagger$ and $\Delta S^\dagger$ for the uncorrected energy and entropy change, respectively.

We first examine the PMF $\Delta F(r)$ between two fully charged polyions with opposite charges as a function of their center-of-mass distance r in the absence of added salt (with $N_C = N_A = 60$, $\xi = 1.03$; see details in *Materials and Methods*). Fig. 1 shows a large free energy decrease as the two chains approach each other, reaching a magnitude of about $400k_BT$ at close contact; this number is very close to that reported by Ou and Muthukumar (76) under the same condition. Without the entropic correction in the electrostatic interaction, Fig. 1*B* shows that complexation is energy driven as most of the free energy decrease comes from the energy, i.e., $-\Delta U^\dagger > T\Delta S^\dagger$. The small entropy increase is likely due to counterion release upon complexation (76, 78). The value of the energy change between the complex and the two separate chains is also in agreement with that reported in ref. 76, and the general conclusion of energy dominance is consistent with previous simulation findings for $\xi < 1.5$ (76, 78, 79). However, when the entropic contribution to the electrostatic interaction is accounted for, the complexation becomes entirely entropy driven, as shown in Fig. 1*C*. The corrected energy contribution is small and unfavorable, consistent with the endothermic behavior observed in experiments (71). *SI Appendix*, Fig. S2 shows that adding salt ($0.01 \sim 0.1M$) to the system weakens the overall driving force as measured by PMF, and the energetic contribution becomes negligible at higher salt concentrations. With the entropic correction, all our results are consistent with experimental observations (71, 75).

Although we have only presented results for $\xi \approx 1.03$, Eq. **8** can be applied to previous simulation data based on continuum

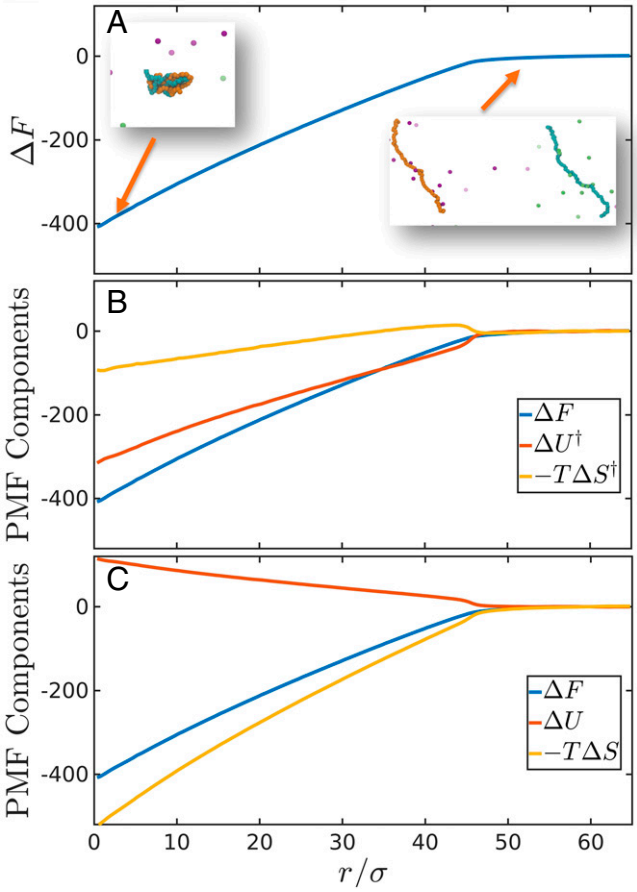

Fig. 1. (*A*) PMF for the complexation of a polycation (orange) and a polyanion (cyan) each with chain length $N = 60$. The small dots in *Inset* are the corresponding counterions. (*B*) Components of the free energy without the electrostatic entropy correction. (*C*) Components of the free energy with the electrostatic entropy correction according to Eq. **8**. The energy unit in all curves is k_BT at room temperature (298.15 K).

electrostatics to extract the electrostatic entropy in broader ranges of ξ. In *SI Appendix*, Fig. S3, we show that using the simulation data in ref. 76, after making the entropic correction in the electrostatic term, the polycation–polyanion complexation becomes strongly entropy driven with only minor energetic contributions in the most experimentally relevant ranges of $\xi(<3)$ for aqueous systems, in agreement with experiments. Furthermore, after the correction, the trend in the enthalpy change (turning from positive to negative) with increasing ξ in the range of $1 < \xi < 3$ is also consistent with experiments (75, 81). Moreover, by comparing the entropy change before and after the correction, we find that the electrostatic entropy is the primary entropic driving force for $\xi < 1.7$.

The PMF of polycation–polyanion complexation can shed useful light on the nature of the dilute phase in polyelectrolyte complex coacervation, which has received considerably less attention than the coacervate phase. In the calculation of phase diagrams, most theories (20–22, 25, 26, 30–32, 91–98) assume the polyions exist as dispersed chains in the dilute phase and consequently predict unphysically low polymer concentration in the supernatant phase. On the other hand, it has long been suggested that the supernatant phase for symmetric polyelectrolyte mixtures should consist primarily of polyion pairs under physically relevant conditions (21, 66, 67, 99). This has been explicitly demonstrated by field-theoretic simulation (100) and theoretical calculation (43) for weakly charged polyelectrolytes

in the absence of counterions and elaborated more recently for the general polyelectrolyte complex coacervation in symmetric mixtures (101). With the calculated PMF for polycation–polyanion complexation, we can quantify the onset concentration for polyion pairing from dispersed polycations and polyanions.

We consider the polycation–polyanion complexation as a chemical reaction:

$$A + C \rightleftharpoons AC, \qquad [9]$$

where A, C, and AC denote polyanion, polycation, and polyanion–polycation pair, respectively. The equilibrium constant K_{eq} is given by

$$K_{eq} = \frac{\rho_{AC}}{\rho_A \cdot \rho_C} = \frac{Q_{AC}}{Q_A Q_C}, \qquad [10]$$

where ρ_α is the concentration of the α specie and Q_α is the corresponding internal partition function (102). The ratio of the partition functions on the right-hand side of Eq. **10** is related to the PMF by

$$\frac{Q_{AC}}{Q_A Q_C} = 4\pi \int_0^{r_{max}} r^2 e^{-\Delta F(r)/k_B T}\, dr, \qquad [11]$$

where r_{max} is the range of the attractive well of the PMF. Noting that $\Delta F(r)$ increases steeply with r, the integral is dominated by contributions near the minimum ($r = 0$), and we may expand $\Delta F(r)$ to linear order by writing $\Delta F(r)/k_B T = \Delta F(0)/k_B T + a(r/\sigma)$, with a being the local slope near the minimum. For the PMF given in Fig. 1, Eq. **11** yields an approximate value for the equilibrium constant $K_{eq} \approx (8\pi/a^3)\sigma^3 e^{-\Delta F(r)(0)/k_B T} \approx 10^{174} nm^3 \approx 10^{150} L$. If we take the onset concentration for the complexation to be $\rho^*_{AC} = \rho^*_A = \rho^*_C$, then we obtain $\rho^*_A = \rho^*_C \approx 10^{-174} M$, an unfathomably small number. The onset concentration increases by many orders of magnitude with increasing salt concentration, but even for the highest salt concentration we studied ($\sim 0.1M$), ρ^*_A is still unphysically low. Thus, except at very high salt concentrations, a dilute mixture of polyanions and polycations will consist of polyion pairs, practically devoid of uncomplexed polyelectrolyte chains.

The value of the complexation free energy obtained from our simulation is comparable to those measured in experiments. On a per monomer basis, the $\sim 400 k_B T$ free energy drop per chain shown in Fig. 1 amounts to 17 kJ/mol per monomer. This number falls in the range of the experimentally reported values (10 to 30 kJ/mol) of the complexation free energy for a series of polyanion and polycation pairs (71, 75). Given the simplicity of the coarse-grained model employed in our work, this level of agreement is quite heartening. In *SI Appendix*, we briefly discuss the effects of chain length and length asymmetry in the pairing free energy for polycation–polyanion complexation (see *SI Appendix*, Fig. S4).

Since the dilute phase of a symmetric mixture of polyanions and polycations is essentially devoid of uncomplexed chains, the relevant species are the polycation–polyanion pairs, whose condensation eventually results in the coacervate. Here we consider the elementary process of the fusion of such polyion pairs. In Fig. 2*A*, we show the PMF between two polyion pairs, each containing one polycation and one polyanion that are both fully charged and have the same chain length $N = 100$, at different added salt concentrations $C_s = 0M \sim 0.15M$.

Because the two polyion pairs have no net macromolecular charges, the primary driving force for their fusion comes from the tendency to decrease the interfacial free energy (43, 101). Consequently, the free energy of fusion is considerably less than the

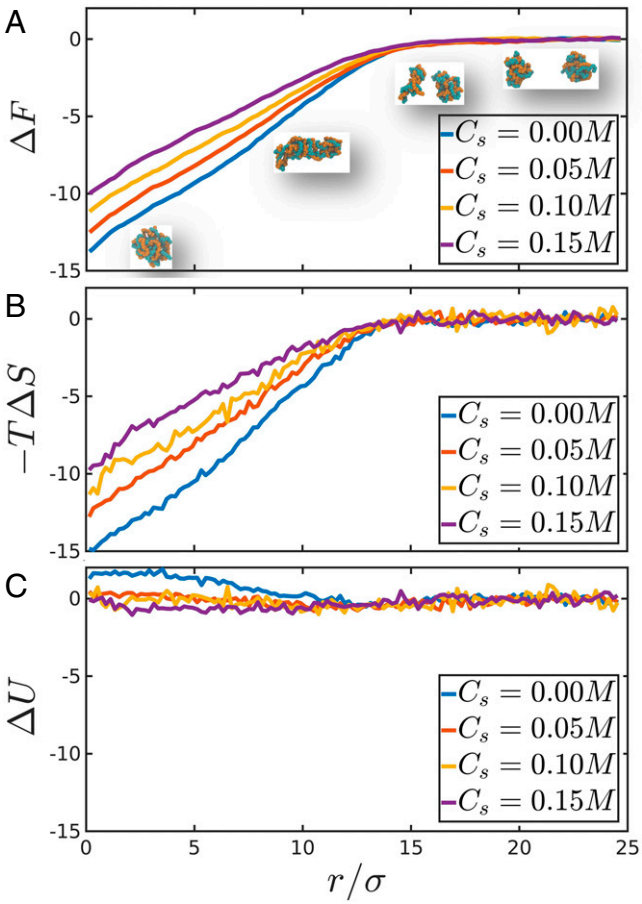

Fig. 2. Thermodynamics driving force for the condensation of two polycation–polyanion pairs under different added salt conditions for $N = 100$. (*A*) PMF ΔF. (*B*) Corrected entropy contribution (Eq. **8**). (*C*) Corrected energy contribution. The energy unit in all curves is $k_B T$ at room temperature (298.15 K).

free energy of the polycation–polyanion complexation discussed earlier; see Fig. 2*A* and compare with Fig. 1. A few representative structures along the fusion pathway are shown in the insets of Fig. 2*A*, where we see two isolated globules at long distances, going through an elongated connected state, to the final fused larger globule.

As in the case of polycation–polyanion complexation, we find that the fusion between two polyion pairs is also driven by entropy (when the corrected entropy expression is used), as shown in Fig. 2 *B* and *C*. The energy contribution is slightly unfavorable for the salt-free system (still with counterions) and becomes less with increasing salt concentration. Although the fusion of two polyion pairs is only part of the overall coacervation process, the trend observed in our simulation is consistent with the enthalpy change during the second stage of coacervation obtained in experiments (71, 73), in that the measured enthalpy change is small and slightly unfavorable, and its magnitude decreases with added salt. Without the entropic correction in the electrostatic interaction, *SI Appendix*, Fig. S5 shows the energetic contribution is significant and comparable to the entropic contribution, which is inconsistent with the slightly endothermic nature of the second stage in coacervation reported in refs. 71, 73.

The PMF between two polyion pairs allows us to estimate the spinodal of the supernatant phase. To this end, we write the osmotic pressure of the supernatant phase due to the polymers as a virial expansion,

$$\Pi = k_B T(\rho + B_2 \cdot \rho^2 + B_3 \rho^3 + \ldots), \qquad [12]$$

where B_2 and B_3 are the second and third osmotic virial coefficients, respectively. B_2 is related to the PMF by (103)

$$B_2 = -2\pi \int (e^{-\Delta F(r)/k_B T} - 1) r^2 dr. \quad [13]$$

Fitting the PMF as a straight line with slope a in the range of the interaction $r \leq D$, where $D \approx 14\sigma$ is the onset distance for appreciable interaction (roughly the onset of contact between the two polyion pair globules, which appears insensitive to the salt concentrations we have examined), B_2 is estimated to be

$$B_2 \approx -\left[\frac{4\pi}{a^3}\sigma^3 e^{-\Delta F(0)/k_B T} - \frac{2\pi}{3}D^3\right]. \quad [14]$$

Invoking the spinodal condition $\partial\Pi/\partial\rho = 0$ and ignoring the contribution from the third virial coefficient [which is presumably positive and not very large (66, 67)], we estimate the concentration of the polyion pairs at the spinodal to be

$$\rho^s \approx -1/(2B_2). \quad [15]$$

For the chain length and salt conditions studied here, the second term on the right-hand side of Eq. **14** is only a small fraction ($\leq 2\%$) of the first term. Therefore, the spinodal concentration is roughly

$$\rho^s \approx \frac{a^3}{4\pi\sigma^3} e^{\Delta F(0)/k_B T}. \quad [16]$$

In the supernatant phase at undersaturated concentrations, and at the binodal, the solution consists primarily of isolated polyion pairs, with much lower concentration of two-pair complexes and higher-order clusters (101). From the PMF shown in Fig. 2*A*, we can obtain the equilibrium constant for the dimerization from two polyion pairs,

$$\frac{\rho_2}{\rho_1^2} \approx (8\pi/a^3)\sigma^3 e^{-\Delta F(0)/k_B T}, \quad [17]$$

where ρ_1 and ρ_2 are the concentration of the polyion pairs and that of the dimers of these pairs (hereafter termed two-pair complex), respectively. As the concentration of polyion pairs ρ_1 increases, ρ_2 increases according to Eq. **17**. For sufficiently high ρ_1, the concentration of the two-pair complexes becomes comparable to that of the polyion pairs. This happens when $\rho_1 \approx \frac{a^3}{8\pi\sigma^3} e^{\Delta F(0)/k_B T}$. Up to a numerical factor of order 1, this is just the spinodal condition given in Eq. **16**. This result is not surprising: since the fusion of two polyion pairs does not involve any kinetic barrier, the only free energy barrier to coacervation is due to the translational entropy loss of the polyion pairs in forming two-pair complexes and higher-order clusters, if we consider the cluster size as the reaction coordinate to nucleation (101, 104). When $\rho_2 \approx \rho_1$, the free energy barrier to cluster growth vanishes—this is the condition of spinodal.

The results for the spinodal concentration are shown in Fig. 3 for the four salt concentrations studied. The spinodal concentration increases with added salt, following the same trend as the binodal shown in both theoretical and experimental phase diagrams; the binodal for the present system, which is not available from these two-pair calculations, is expected to lie below the curve shown in Fig. 3. Between the binodal and the spinodal, the system is in the metastable state, from which coacervation proceeds by nucleation and growth, with vanishing barrier at the spinodal. In practice, the metastable state can no longer exist when

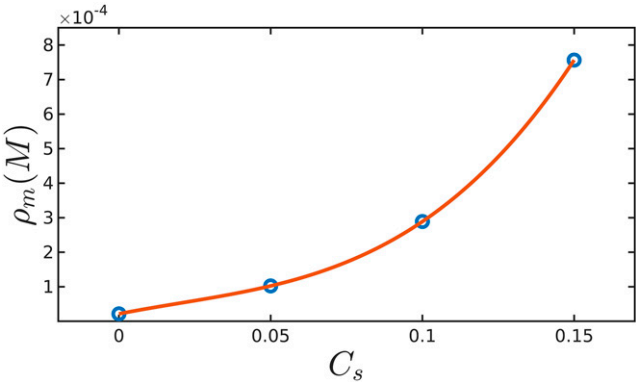

Fig. 3. Spinodal concentration of the polymers for the dilute branch under different added salt conditions. The polymer concentration is measured using the total number of monomers.

the nucleation barrier becomes a few $k_B T$ due to the enhanced fluctuation near the spinodal (101, 105–107).

While the PMF becomes significant for $r \lesssim D$ (the contact distance), a close inspection of the curves in Fig. 2*A* reveals a faint attraction at $r > D$. This attraction arises from the mutually induced polarization of the two polyion-pair globules. To quantify this induced polarization effect, we examine the fluctuation in the net dipole of each globule, as well as the overall dipole of the two-globule system.

For each pair, the electric dipole moment is given by $\vec{P}_\alpha = \sum_i q_{\alpha,i}\vec{r}_{\alpha,i}$, where $q_{\alpha,i}$ is the charge on monomer i and $r_{\alpha,i}$ is its vector position, and the sum is over all monomers in pair α ($\alpha = 1, 2$). The total dipole of the system is then $\vec{P} = \vec{P}_1 + \vec{P}_2$. We calculate the projection of these dipole moment onto the center-of-mass vector between the pairs:

$$P_{||,\alpha} = \vec{P}_\alpha \cdot \hat{R}_{12}, \quad [18]$$

where $\hat{R}_{12}$ is the unit vector of the center of mass between the two pairs defined as $\hat{R}_{12} = (\vec{R}_{c,2} - \vec{R}_{c,1})/|\vec{R}_{c,2} - \vec{R}_{c,1}|$, with $\vec{R}_{c,\alpha}$ being the instantaneous center of mass position of pair α. Because of symmetry, $\langle P_{||,\alpha}\rangle = 0$. Thus, we quantify the fluctuation by the second moment $\langle P^2_{||,\alpha}\rangle$ and $\langle P^2_{||}\rangle$. Furthermore, we calculate the dipole correlation between the two pairs $\langle P_{||,1}P_{||,2}\rangle$

$$\langle P_{||,1}P_{||,2}\rangle = \frac{1}{2}[\langle P^2_{||}\rangle - \langle P^2_{||,1}\rangle - \langle P^2_{||,2}\rangle]. \quad [19]$$

In Fig. 4 *A* and *B*, we show the fluctuation in the total dipole moment and the dipole–dipole correlation between the two polyion pairs. We see that the system dipole fluctuation becomes appreciable at $r/\sigma \lesssim 20$, indicating mutually induced polarization well beyond the contact distance. This induced polarization is more easily seen in the correlation $\langle P_{||,1}P_{||,2}\rangle$ shown in Fig. 4*B*. The large increase in the correlation as r decreases below 20σ indicates that the dipoles from the two polyion pairs point in the same direction. Furthermore, the polarization increases with increasing salt concentration; this can be understood by the decrease in the density of the polyion-pair globule (*SI Appendix*, Fig. S7) and the accompanying decrease in the interfacial tension with added salt (93, 108), which makes the globule more deformable. The globule shape anisotropy follows similar trend as the polarization (*SI Appendix*, Fig. S6).

Beyond the fusion between two polyion pairs, coacervation involves the condensation into larger clusters which eventually leads to macroscopic phase separation. It is therefore of interest

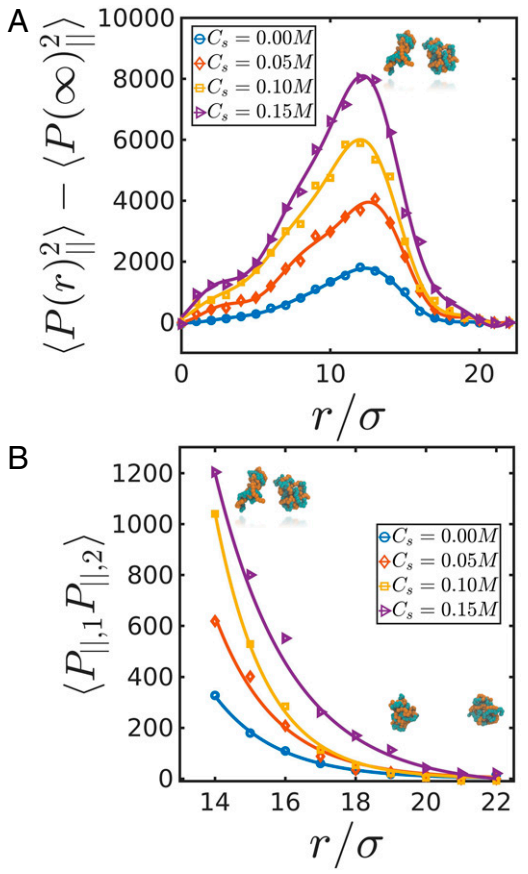

Fig. 4. (*A*) Fluctuation of the longitudinal component of the polarization $\langle P^2_{||}\rangle$ as a function of the center-of-mass distance between the two pairs, relative to that at infinite distance. The markers represent the simulation data, and the curves are fitted to guide the eye. (*B*) Polarization correlation between the two polyion globules $\langle P_{||,1} P_{||,2}\rangle$ as a function of the center-of-mass distance between the two pairs at $r/\sigma \geq 14$, where the two pairs weakly attract each other prior to contact. The curves are fitted to guide the eye.

to examine how the structural properties evolve as the cluster size increases. To this end, we study and compare clusters with sizes ranging from 1 to 10 polyion pairs.

Fig. 5 *A*–*D* show the polymer radial density profile. For each cluster, the polymer density within the cluster decreases with increasing salt, consistent with the behavior of the density on the coacervate branch of the phase diagram observed in experiments and predicted by theories. Thus, the structure of the interior of these clusters is similar to the bulk coacervate phase. Interestingly, the polymer density in the interior of the clusters deceases with increasing cluster size, as shown in the comparison in Fig. 5 *A*–*D*, where the four figures share the same ordinate coordinate (y axis); this is seen more clearly in *SI Appendix*, Fig. S7. The higher density for smaller clusters is due to the effect of the interfacial tension, which results in increased Laplace pressure inside the cluster with decreasing cluster radius R according to $\Delta P_L = 2\gamma/R$, where γ is the surface tension. In addition, visual inspection of the cluster morphology shows that the smaller clusters tend to be more rounded, implying a higher interfacial tension. Indeed, by examining the decay of the density profile in Fig. 5 *A*–*D*, we can see that the larger clusters have larger interfacial width. All these observations are consistent with theoretical predictions from a recent study (108).

We next examine the salt partition inside and outside the clusters. Fig. 5 *E*–*H* shows the density profile ρ_i of the small ions (counterion + salt), normalized by the ion density outside the cluster ρ_i^I. The salt is lower inside the cluster, suggesting a negative tie line in the phase diagram, which is consistent with most theories and experiments. Interestingly, the ion concentration shows a peak just outside of the cluster at low salt concentrations (salt-free and $C_s = 0.05M$); this feature is in agreement with the theoretical prediction in ref. 108.

In conclusion, by focusing on the elementary process of the complexation between a polycation and a polyanion and the subsequent fusion of two polyion pairs, we have elucidated the driving force and pathway in polyelectrolyte complex coacervation in symmetric polyelectrolyte mixtures. By accounting for the electrostatic entropy, which is implicit in the coarse-grained models, we resolve an apparent discrepancy between experiments and previous coarse-grained simulations regarding the thermodynamic driving force. Our analysis shows that both the polycation–polyanion complexation and the pair–pair condensation are driven almost entirely by entropy, in agreement with experimental results. For fully charged PE with moderately long chain lengths, we estimate that under most conditions away from the critical point, the concentration of uncomplexed polyions is vanishingly small; the supernatant phase consists predominantly of polyion pairs. From the PMF between two polyion pairs, we are able to estimate the spinodal concentration of the supernatant phase. Finally, we show there exists a weak attraction between two macromolecular neutral polyion-pair globules prior to contact due to mutually induced polarization; this action-at-a-distance provides the initial driving force for the fusion of the polyion pairs, eventually leading to the formation of macroscopic coacervate phase.

While the prevailing view in the polyelectrolyte community holds that counterion release is the primary entropic contribution to the thermodynamic driving force for polyelectrolyte coacervation (61–63, 72, 76), our results show that a significant entropic component in the free energy change comes from the temperature dependence in the dielectric constant of water, and this electrostatic entropy is the main contribution to the overall entropy change in the regime of weak to intermediate electrostatic strength. More generally, our results emphasize that coarse-grained effective potentials inherently include entropic contributions (109) due to solvent reorganization, and care must be taken when interpreting experimental thermodynamic data using coarse-grained simulations.

We end our discussion with a few remarks on the limitations of the simulation model used here (and in many other coarse-grained simulations of electrolyte and polyelectrolyte systems). The treatment of ion–ion interactions using a uniform bulk dielectric constant has two clear drawbacks. First, it does not capture the discrete nature of the solvent molecules at short ion–ion separations. Second, high polymer and salt concentration will result in changes in the local dielectric permittivity. The first effect would require a model with explicit solvent, while the second would require a better description of the local polarization due to polymer or ion enrichment. Although computational methods for including both effects exist (110–112) (in addition to fully atomistic models), accounting for these effects in the context of polyelectrolyte complex coacervation is computationally demanding and is beyond the scope of our work. A closely related effect is the change in the local hydration structure of the ions due to high temperature and strong binding by multivalent ions (75, 113–120), which can result in substantial entropy changes related to water release (121). Such an effect cannot be described with a simple dielectric continuum treatment. However, within the framework of the primitive model for electrolytes/polyelectrolytes,

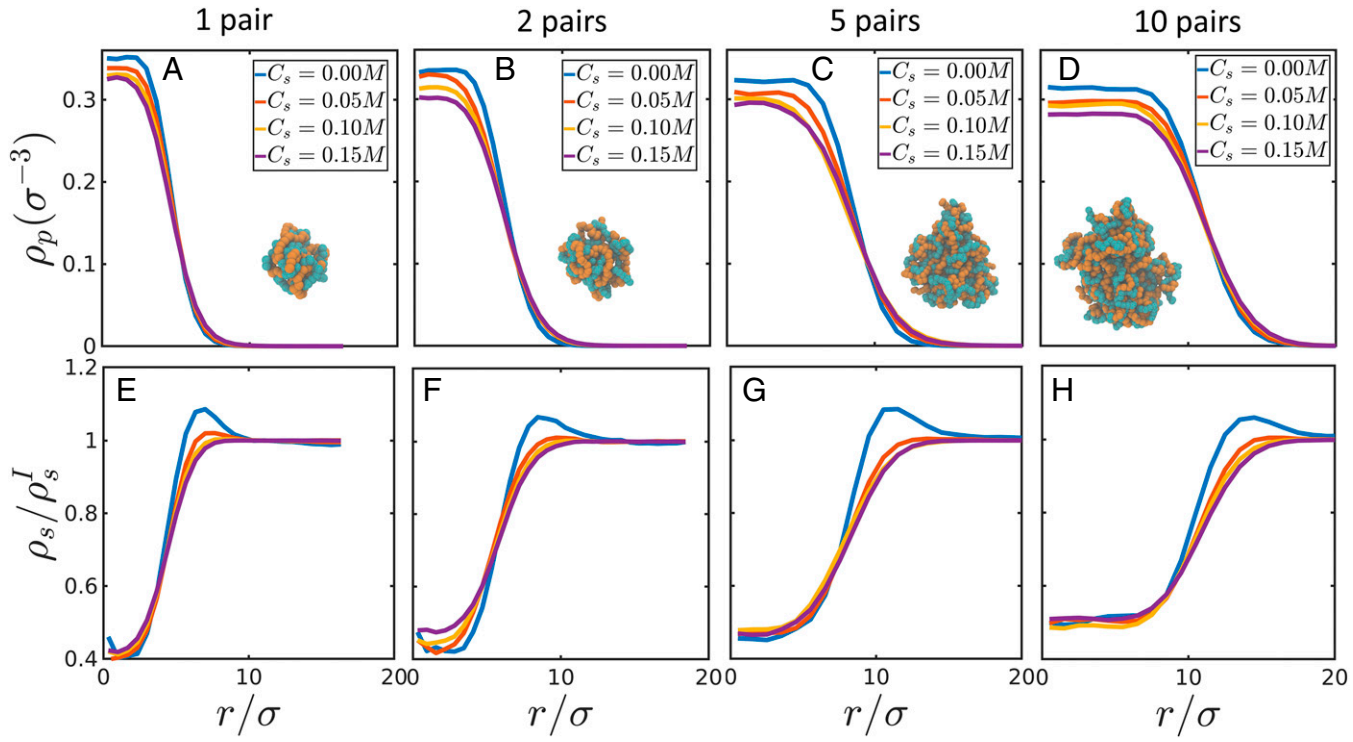

Fig. 5. (*A–D*) Radial monomer density profile for neutral polyion clusters with varying sizes at different salt concentrations. (*E–H*) Corresponding small-ion density profile for each cluster.

it is possible to capture many of the structural features of polyelectrolyte complex coacervation due to divalent ions (122–124) by introducing a phenomenological binding energy (125). Despite these considerations, we note that the implicit-solvent, dielectric continuum description of charged systems has been very successful in modeling a wide range of systems involving electrolyte and polyelectrolyte solutions even at fairly high salt concentrations (126). In view of the overall agreement between our simulation results and experimental findings, we expect that for weak-to-moderate electrostatic strengths with monovalent salt ions at room temperature, these additional effects will modify but not fundamentally alter the main results of this work.

Materials and Methods

The monomers and small ions in our simulation are represented as beads interacting with the shifted-truncated Lennard-Jones potential of the form $U^{ij}_{WCA}(r_{ij}) = 4\varepsilon_{ij}[(\frac{\sigma_{ij}}{r_{ij}})^{12} - (\frac{\sigma_{ij}}{r_{ij}})^{6} + \frac{1}{4}]$ with a cutoff distance $r_{cut} = 2^{1/6}\sigma_{ij}$. We set $\sigma_{ij} = \sigma$ and $\varepsilon_{ij} = k_BT$. Neighboring beads along the polymer chains are subjected to the FENE potential given by $U^{ij}_{FENE}(r_{ij}) = \frac{1}{2}K_{bond}R_0^2\ln[1 - (\frac{r_{ij}}{R_0})^2]$, with $K_{bond} = 30k_BT/\sigma^2$ and $R_0 = 1.5\sigma$. All the beads have the same mass m and size σ. This setup reproduces a good solvent condition for neutral polymers. With k_BT being the energy scale in these potentials, these nonelectrostatic interactions should be considered as entropic in nature. However, since they contribute minimally to the PMF (*SI Appendix*, Fig. S1), the precise designation of these nonelectrostatic interaction energies is immaterial.

The polyelectrolytes are linear chains with every monomer carrying a unit charge $+e$ or $-e$. Each charged polymer bead has a corresponding counterion bead carrying the opposite unit charge. Salt ions are modeled as monovalent beads having the same identity as the counterions. The long-range electrostatic interaction is given by $E^{ij}_{el} = k_BT\frac{l_Bq_iq_j}{r_{ij}}$, where the Bjerrum length is given by $l_B = e^2/(4\pi\epsilon k_BT)$. For water at $T = 298.15$ K, $l_B \approx 0.7$ nm. This value is roughly the diameter of common hydrated monovalent ions in water (127). Therefore, we set $\sigma = l_B$ in our simulation. The average equilibrium bond length is $l \approx 0.97\sigma$; thus, the electrostatic strength $\xi = l_B/l \approx 1.03$. At this ξ, without considering the electrostatic entropy, the complexation of two oppositely charged PEs was reported to be energy driven in previous simulations (76, 78).

All our simulations are performed in the canonical ensemble with a Langevin thermostat using the LAMMPS (Large-scale Atomic/Molecular Massively Parallel Simulator) platform. The simulation time scale is given by $\tau = \sqrt{m\sigma^2/k_BT} = 1$. The positions and velocities of the beads are updated with an integration time step $\Delta t = 0.01\tau$. For the PMF calculation of the two-chain systems, the simulation box is set to $130\sigma \times 130\sigma \times 130\sigma$. This is the same setup as that in refs. 76 and 78. For the two-pair systems, the simulation box is $45\sigma \times 45\sigma \times 45\sigma$. Note that each polycation–polyanion pair exists as a neutral globule, which allows us to use a smaller box size to study the pair–pair condensation PMF. Each structural unit (a polyelectrolyte chain or polyion pair) is equilibrated for $10^5\tau$ (10^7 time steps) before performing the PMF calculations. The PMF calculations are carried out by the adaptive bias force algorithm (128, 129) implemented in LAMMPS (130). The coordinate of the PMF is taken to be the center-of-mass distance between the two structural units (chains or pairs). The distance range r is $0\sigma \sim 65\sigma$ for the two-chain case and $0\sigma \sim 25\sigma$ for the two-pair case. To improve the efficiency of the PMF calculations (129), the distance range is divided into 10 consecutive windows. Each window is further divided into bins with equal width 0.5σ for the two-chain case and 0.2σ for the two-pair system. For each window, we perform the simulation for $2 \times 10^6\tau$ to get convergence. To avoid nonequilibrium effects, we use the scheme documented by Miao et al. (131) to set the sampling time prior to applying the adaptive bias force in each bin. The PMF is calculated on the fly by integrating the biased force between neighboring bins. The PMF in most windows reaches convergence before $2 \times 10^5\tau$, after which the relative free energy change in each window is less than 1% for an additional time duration of $10^5\tau$.

Data, Materials, and Software Availability. All study data are included in the article and/or *SI Appendix*.

ACKNOWLEDGMENTS. This research is supported by funding from Hong Kong Quantum AI Lab Ltd. We thank the general computation time allocated by the resources of the Center for Functional Nanomaterials, which is a US Department of Energy Office of Science User Facility, at Brookhaven National Laboratory under Contract DE-SC0012704. We thank Prof. M. Muthukumar for bringing our attention to his forthcoming book.

1. F. W. Tiebackx, Gleichzeitige Ausflockung zweier Kolloide. *Z. Chem. Ind. Koll.* **8**, 198–201 (1911).
2. B. de Jong, H. R. Kruyt, Coacervation. *Proc. R. Acad. Amsterdam* **32**, 849–856 (1929).
3. C. P. Brangwynne, P. Tompa, R. V. Pappu, Polymer physics of intracellular phase transitions. *Nat. Phys.* **11**, 899–904 (2015).
4. T. J. Nott *et al.*, Phase transition of a disordered nuage protein generates environmentally responsive membraneless organelles. *Mol. Cell* **57**, 936–947 (2015).
5. S. Alberti, A. Gladfelter, T. Mittag, Considerations and challenges in studying liquid-liquid phase separation and biomolecular condensates. *Cell* **176**, 419–434 (2019).
6. N. A. Yewdall, A. A. André, T. Lu, E. Spruijt, Coacervates as models of membraneless organelles. *Curr. Opin. Colloid Interface Sci.* **52**, 101416 (2021).
7. B. P. Lee, P. B. Messersmith, J. N. Israelachvili, J. H. Waite, Mussel-inspired adhesives and coatings. *Annu. Rev. Mater. Res.* **41**, 99–132 (2011).
8. W. Wei *et al.*, A mussel-derived one component adhesive coacervate. *Acta Biomater.* **10**, 1663–1670 (2014).
9. J. H. Waite, Mussel adhesion–Essential footwork. *J. Exp. Biol.* **220**, 517–530 (2017).
10. H. J. Kim, B. Yang, T. Y. Park, S. Lim, H. J. Cha, Complex coacervates based on recombinant mussel adhesive proteins: Their characterization and applications. *Soft Matter* **13**, 7704–7716 (2017).
11. R. J. Stewart, C. S. Wang, I. T. Song, J. P. Jones, The role of coacervation and phase transitions in the sandcastle worm adhesive system. *Adv. Colloid Interface Sci.* **239**, 88–96 (2017).
12. K. M. Jin, Y. H. Kim, Injectable, thermo-reversible and complex coacervate combination gels for protein drug delivery. *J. Control. Release* **127**, 249–256 (2008).
13. N. R. Johnson, Y. Wang, Controlled delivery of heparin-binding EGF-like growth factor yields fast and comprehensive wound healing. *J. Control. Release* **166**, 124–129 (2013).
14. W. C. Blocher, S. L. Perry, Complex coacervate-based materials for biomedicine. *Wiley Interdiscip. Rev. Nanomed. Nanobiotechnol.* **9**, e1442 (2017).
15. H. Shao, R. J. Stewart, Biomimetic underwater adhesives with environmentally triggered setting mechanisms. *Adv. Mater.* **22**, 729–733 (2010).
16. R. J. Stewart, C. S. Wang, H. Shao, Complex coacervates as a foundation for synthetic underwater adhesives. *Adv. Colloid Interface Sci.* **167**, 85–93 (2011).
17. M. Dompé *et al.*, Thermoresponsive complex coacervate-based underwater adhesive. *Adv. Mater.* **31**, e1808179 (2019).
18. M. Dompé *et al.*, Hybrid complex coacervate. *Polymers (Basel)* **12**, 320 (2020).
19. M. Vahdati, F. J. Cedano-Serrano, C. Creton, D. Hourdet, Coacervate-based underwater adhesives in physiological conditions. *ACS Appl. Polym. Mater.* **2**, 3397–3410 (2020).
20. J. T. G. Overbeek, M. J. Voorn, Phase separation in polyelectrolyte solutions; theory of complex coacervation. *J. Cell. Physiol. Suppl.* **49** (suppl. 1), 7–22, (1957).
21. V. Yu Borue, I. Ya Erukhimovich, A statistical theory of globular polyelectrolyte complexes. *Macromolecules* **23**, 3625–3632 (1990).
22. A. Kudlay, A. V. Ermoshkin, M. Olvera de la Cruz, Complexation of oppositely charged polyelectrolytes: Effect of ion pair formation. *Macromolecules* **37**, 9231–9241 (2004).
23. M. Castelnovo, J. F. Joanny, Complexation between oppositely charged polyelectrolytes: Beyond the random phase approximation. *Eur. Phys. J. E* **6**, 377–386 (2001).
24. J. Lee, Y. O. Popov, G. H. Fredrickson, Complex coacervation: A field theoretic simulation study of polyelectrolyte complexation. *J. Chem. Phys.* **128**, 224908 (2008).
25. S. L. Perry, C. E. Sing, PRISM-based theory of complex coacervation: Excluded volume versus chain correlation. *Macromolecules* **48**, 5040–5053 (2015).
26. J. Qin, J. J. de Pablo, Criticality and connectivity in macromolecular charge complexation. *Macromolecules* **49**, 8789–8800 (2016).
27. M. Radhakrishna *et al.*, Molecular connectivity and correlation effects on polymer coacervation. *Macromolecules* **50**, 3030–3037 (2017).
28. K. Shen, Z.-G. Wang, Polyelectrolyte chain structure and solution phase behavior. *Macromolecules* **51**, 1706–1717 (2018).
29. A. M. Rumyantsev, E. B. Zhulina, O. V. Borisov, Complex coacervate of weakly charged polyelectrolytes: Diagram of states. *Macromolecules* **51**, 3788–3801 (2018).
30. P. Zhang, K. Shen, N. M. Alsaifi, Z.-G. Wang, Salt partitioning in complex coacervation of symmetric polyelectrolytes. *Macromolecules* **51**, 5586–5593 (2018).
31. A. Kudlay, M. Olvera de la Cruz, Precipitation of oppositely charged polyelectrolytes in salt solutions. *J. Chem. Phys.* **120**, 404–412 (2004).
32. T. K. Lytle, C. E. Sing, Transfer matrix theory of polymer complex coacervation. *Soft Matter* **13**, 7001–7012 (2017).
33. L. Li *et al.*, Phase behavior and salt partitioning in polyelectrolyte complex coacervates. *Macromolecules* **51**, 2988–2995 (2018).
34. S. P. O. Danielsen, J. McCarty, J. E. Shea, K. T. Delaney, G. H. Fredrickson, Molecular design of self-coacervation phenomena in block polyampholytes. *Proc. Natl. Acad. Sci. U.S.A.* **116**, 8224–8232 (2019).
35. J. Huang, J. E. Laaser, Charge density and hydrophobicity-dominated regimes in the phase behavior of complex coacervates. *ACS Macro Lett.* **10**, 1029–1034 (2021).
36. C. W. Pak *et al.*, Sequence determinants of intracellular phase separation by complex coacervation of a disordered protein. *Mol. Cell* **63**, 72–85 (2016).
37. A. M. Rumyantsev *et al.*, Controlling complex coacervation via random polyelectrolyte sequences. *ACS Macro Lett.* **8**, 1296–1302 (2019).
38. L. W. Chang *et al.*, Sequence and entropy-based control of complex coacervates. *Nat. Commun.* **8**, 1273 (2017).
39. J. J. Madinya, L. W. Chang, S. L. Perry, C. E. Sing, Sequence-dependent self-coacervation in high charge-density polyampholytes. *Mol. Syst. Des. Eng.* **5**, 632–644 (2020).
40. N. A. Zervoudis, A. C. Obermeyer, The effects of protein charge patterning on complex coacervation. *Soft Matter* **17**, 6637–6645 (2021).
41. J. B. Schlenoff, M. Yang, Z. A. Digby, Q. Wang, Ion content of polyelectrolyte complex coacervates and the Donnan equilibrium. *Macromolecules* **52**, 9149–9159 (2019).
42. S. P. O. Danielsen, S. Panyukov, M. Rubinstein, Ion pairing and the structure of gel coacervates. *Macromolecules* **53**, 9420–9442 (2020).
43. A. M. Rumyantsev, I. I. Potemkin, Explicit description of complexation between oppositely charged polyelectrolytes as an advantage of the random phase approximation over the scaling approach. *Phys. Chem. Chem. Phys.* **19**, 27580–27592 (2017).
44. P. Zhang, N. M. Alsaifi, J. Wu, Z.-G. Wang, Polyelectrolyte complex coacervation: Effects of concentration asymmetry. *J. Chem. Phys.* **149**, 163303 (2018).
45. S. Friedowitz *et al.*, Looping-in complexation and ion partitioning in nonstoichiometric polyelectrolyte mixtures. *Sci. Adv.* **7**, eabg8654 (2021).
46. S. V. Bobbili, S. T. Milner, Closed-loop phase behavior of nonstoichiometric coacervates in coarse-grained simulations. *Macromolecules* **55**, 511–516 (2022).
47. S. Chen, P. Zhang, Z. G. Wang, Complexation between oppositely charged polyelectrolytes in dilute solution: Effects of charge asymmetry. *Macromolecules* **55**, 3898–3909 (2022).
48. S. Adhikari, M. A. Leaf, M. Muthukumar, Polyelectrolyte complex coacervation by electrostatic dipolar interactions. *J. Chem. Phys.* **149**, 163308 (2018).
49. J. D. Tang, S. R. Caliari, K. J. Lampe, Temperature-dependent complex coacervation of engineered elastin-like polypeptide and hyaluronic acid polyelectrolytes. *Biomacromolecules* **19**, 3925–3935 (2018).
50. S. Adhikari, V. M. Prabhu, M. Muthukumar, Lower critical solution temperature behavior in polyelectrolyte complex coacervates. *Macromolecules* **52**, 6998–7004 (2019).
51. Z. Ye, S. Sun, P. Wu, Distinct cation-anion interactions in the UCST and LCST behavior of polyelectrolyte complex aqueous solutions. *ACS Macro Lett.* **9**, 974–979 (2020).
52. A. Narayanan, J. R. Menefee, Q. Liu, A. Dhinojwala, A. Joy, Lower critical solution temperature-driven self-coacervation of nonionic polyester underwater adhesives. *ACS Nano* **14**, 8359–8367 (2020).
53. A. S. Ylitalo, C. Balzer, P. Zhang, Z.-G. Wang, Electrostatic correlations and temperature-dependent dielectric constant can model LCST in polyelectrolyte complex coacervation. *Macromolecules* **54**, 11326–11337 (2021).
54. F. Weinbreck, R. de Vries, P. Schrooyen, C. G. de Kruif, Complex coacervation of whey proteins and gum arabic. *Biomacromolecules* **4**, 293–303 (2003).
55. P. Jha, P. Desai, J. Li, R. Larson, pH and salt effects on the associative phase separation of oppositely charged polyelectrolytes. *Polymers (Basel)* **6**, 1414–1436 (2014).
56. M. Ghasemi, R. G. Larson, Role of electrostatic interactions in charge regulation of weakly dissociating polyacids. *Prog. Polym. Sci.* **112**, 101322 (2021).
57. A. R. Knoerdel, W. C. Blocher McTigue, C. E. Sing, Transfer matrix model of pH effects in polymeric complex coacervation. *J. Phys. Chem. B* **125**, 8965–8980 (2021).
58. S. Friedowitz, J. Qin, Reversible ion binding for polyelectrolytes with adaptive conformations. *AIChE J.* **67**, e17426 (2021).
59. M. Lee, S. L. Perry, R. C. Hayward, Complex coacervation of polymerized ionic liquids in non-aqueous solvents. *ACS Polym. Au* **1**, 100–106 (2021).
60. L. Li *et al.*, Effect of solvent quality on the phase behavior of polyelectrolyte complexes. *Macromolecules* **54**, 105–114 (2021).
61. C. E. Sing, Development of the modern theory of polymeric complex coacervation. *Adv. Colloid Interface Sci.* **239**, 2–16 (2017).
62. M. Muthukumar, 50th anniversary perspective: A perspective on polyelectrolyte solutions. *Macromolecules* **50**, 9528–9560 (2017).
63. C. E. Sing, S. L. Perry, Recent progress in the science of complex coacervation. *Soft Matter* **16**, 2885–2914 (2020).
64. A. M. Rumyantsev, N. E. Jackson, J. J. de Pablo, Polyelectrolyte complex coacervates: Recent developments and new frontiers. *Annu. Rev. Condens. Matter Phys.* **12**, 155–176 (2021).
65. V. M. Prabhu, Interfacial tension in polyelectrolyte systems exhibiting associative liquid–liquid phase separation. *Curr. Opin. Colloid Interface Sci.* **53**, 101422 (2021).
66. K. I. Tainaka, Study of complex coacervation in low concentration by virial expansion method. I. Salt free systems. *J. Phys. Soc. Jpn.* **46**, 1899–1906 (1979).
67. K. I. Tainaka, Effect of counterions on complex coacervation. *Biopolymers* **19**, 1289–1298 (1980).
68. M. Girard, S. L. Turgeon, S. F. Gauthier, Thermodynamic parameters of beta-lactoglobulin-pectin complexes assessed by isothermal titration calorimetry. *J. Agric. Food Chem.* **51**, 4450–4455 (2003).
69. X. Feng, M. Leduc, R. Pelton, Polyelectrolyte complex characterization with isothermal titration calorimetry and colloid titration. *Colloids Surf. A Physicochem. Eng. Asp.* **317**, 535–542 (2008).
70. L. Aberkane, J. Jasniewski, C. Gaiani, J. Scher, C. Sanchez, Thermodynamic characterization of acacia gum-beta-lactoglobulin complex coacervation. *Langmuir* **26**, 12523–12533 (2010).
71. D. Priftis, N. Laugel, M. Tirrell, Thermodynamic characterization of polypeptide complex coacervation. *Langmuir* **28**, 15947–15957 (2012).
72. A. B. Kayitmazer, Thermodynamics of complex coacervation. *Adv. Colloid Interface Sci.* **239**, 169–177 (2017).
73. D. Priftis, K. Megley, N. Laugel, M. Tirrell, Complex coacervation of poly(ethylene-imine)/polypeptide aqueous solutions: Thermodynamic and rheological characterization. *J. Colloid Interface Sci.* **398**, 39–50 (2013).
74. C. B. Bucur, Z. Sui, J. B. Schlenoff, Ideal mixing in polyelectrolyte complexes and multilayers: Entropy driven assembly. *J. Am. Chem. Soc.* **128**, 13690–13691 (2006).
75. J. Fu, J. B. Schlenoff, Driving forces for oppositely charged polyion association in aqueous solutions: Enthalpic, entropic, but not electrostatic. *J. Am. Chem. Soc.* **138**, 980–990 (2016).
76. Z. Ou, M. Muthukumar, Entropy and enthalpy of polyelectrolyte complexation: Langevin dynamics simulations. *J. Chem. Phys.* **124**, 154902 (2006).
77. R. M. Elder, T. Emrick, A. Jayaraman, Understanding the effect of polylysine architecture on DNA binding using molecular dynamics simulations. *Biomacromolecules* **12**, 3870–3879 (2011).
78. V. S. Rathee, H. Sidky, B. J. Sikora, J. K. Whitmer, Role of associative charging in the entropy-energy balance of polyelectrolyte complexes. *J. Am. Chem. Soc.* **140**, 15319–15328 (2018).
79. A. N. Singh, A. Yethiraj, Driving force for the complexation of charged polypeptides. *J. Phys. Chem. B* **124**, 1285–1292 (2020).
80. A. N. Singh, A. Yethiraj, Liquid-liquid phase separation as the second step of complex coacervation. *J. Phys. Chem. B* **125**, 3023–3031 (2021).
81. N. Laugel *et al.*, Relationship between the growth regime of polyelectrolyte multilayers and the polyanion/polycation complexation enthalpy. *J. Phys. Chem. B* **110**, 19443–19449 (2006).
82. Q. Wang, J. B. Schlenoff, The polyelectrolyte complex/coacervate continuum. *Macromolecules* **47**, 3108–3116 (2014).
83. A. S. Michaels, Polyelectrolyte complexes. *Ind. Eng. Chem.* **57**, 32–40 (1965).
84. C. G. Malmberg, A. A. Maryott, Dielectric constant of water from 0° to 100°. *J. Res. Natl. Bur. Stand.* **56**, 1–8 (1956).
85. S. Ali, M. Bleuel, V. M. Prabhu, Lower critical solution temperature in polyelectrolyte complex coacervates. *ACS Macro Lett.* **8**, 289–293 (2019).
86. Y. Ma, S. Ali, V. M. Prabhu, Enhanced concentration fluctuations in model polyelectrolyte coacervate mixtures along a salt isopleth phase diagram. *Macromolecules* **54**, 11338–11350 (2021).
87. H. Fröhlich, *Theory of Dielectrics: Dielectric Constant and Dielectric Loss* (Clarendon Press, Oxford, 1958).

88. M. Murugappan, *Physics of Charged Macromolecules: Synthetic and Biological Systems* (Cambridge University Press, Cambridge, United Kingdom, in press).
89. L. Onsager, Electric moments of molecules in liquids. *J. Am. Chem. Soc.* **58**, 1486–1493 (1936).
90. J. G. Kirkwood, The dielectric polarization of polar liquids. *J. Chem. Phys.* **7**, 911–919 (1939).
91. N. P. Shusharina, E. B. Zhulina, A. V. Dobrynin, M. Rubinstein, Scaling theory of diblock polyampholyte solutions. *Macromolecules* **38**, 8870–8881 (2005).
92. Z. Wang, M. Rubinstein, Regimes of conformational transitions of a diblock polyampholyte. *Macromolecules* **39**, 5897–5912 (2006).
93. J. Qin *et al.*, Interfacial tension of polyelectrolyte complex coacervate phases. *ACS Macro Lett.* **3**, 565–568 (2014).
94. P. Zhang, N. M. Alsaifi, J. Wu, Z.-G. Wang, Salting-out and salting-in of polyelectrolyte solutions: A liquid-state theory study. *Macromolecules* **49**, 9720–9730 (2016).
95. A. Salehi, R. G. Larson, A molecular thermodynamic model of complexation in mixtures of oppositely charged polyelectrolytes with explicit account of charge association/dissociation. *Macromolecules* **49**, 9706–9719 (2016).
96. M. Rubinstein, Q. Liao, S. Panyukov, Structure of liquid coacervates formed by oppositely charged polyelectrolytes. *Macromolecules* **51**, 9572–9588 (2018).
97. A. M. Rumyantsev, J. J. de Pablo, Liquid crystalline and isotropic coacervates of semiflexible polyanions and flexible polycations. *Macromolecules* **52**, 5140–5156 (2019).
98. G. M. C. Ong, C. E. Sing, Mapping the phase behavior of coacervate-driven self-assembly in diblock copolyelectrolytes. *Soft Matter* **15**, 5116–5127 (2019).
99. A. Veis, C. Aranyi, Phase separation in polyelectrolyte systems. I. Complex coacervation of gelatin. *J. Phys. Chem.* **64**, 1203–1210 (1960).
100. K. T. Delaney, G. H. Fredrickson, Theory of polyelectrolyte complexation–Complex coacervates are self-coacervates. *J. Chem. Phys.* **146**, 224902 (2017).
101. P. Zhang, Z.-G. Wang, Supernatant phase in polyelectrolyte complex coacervation: Cluster formation, binodal, and nucleation. *Macromolecules* **55**, 3910–3923 (2022).
102. C. N. Likos, Effective interactions in soft condensed matter physics. *Phys. Rep.* **348**, 267–439 (2001).
103. Z.-G. Wang, 50th anniversary perspective: Polymer conformation–A pedagogical review. *Macromolecules* **50**, 9073–9114 (2017).
104. R. Wang, Z.-G. Wang, Theory of polymers in poor solvent: Phase equilibrium and nucleation behavior. *Macromolecules* **45**, 6266–6271 (2012).
105. K. Binder, Collective diffusion, nucleation, and spinodal decomposition in polymer mixtures. *J. Chem. Phys.* **79**, 6387–6409 (1983).
106. K. Binder, Nucleation barriers, spinodals, and the Ginzburg criterion. *Phys. Rev. A* **29**, 341–349 (1984).
107. Z.-G. Wang, Concentration fluctuation in binary polymer blends: χ parameter, spinodal and Ginzburg criterion. *J. Chem. Phys.* **117**, 481–500 (2002).
108. P. Zhang, Z.-G. Wang, Interfacial structure and tension of polyelectrolyte complex coacervates. *Macromolecules* **54**, 10994–11007 (2021).
109. A. Ben-Shaul, Entropy, energy, and bending of DNA in viral capsids. *Biophys. J.* **104**, L15–L17 (2013).
110. D. J. Grzetic, K. T. Delaney, G. H. Fredrickson, Field-theoretic study of salt-induced order and disorder in a polarizable diblock copolymer. *ACS Macro Lett.* **8**, 962–967 (2019).
111. A. A. Gavrilov, Dissipative particle dynamics for systems with polar species: Interactions in dielectric media. *J. Chem. Phys.* **152**, 164101 (2020).
112. A. A. Gavrilov, E. Y. Kramarenko, Two contributions to the dielectric response of polar liquids. *J. Chem. Phys.* **154**, 116101 (2021).
113. J. B. Schlenoff, A. H. Rmaile, C. B. Bucur, Hydration contributions to association in polyelectrolyte multilayers and complexes: Visualizing hydrophobicity. *J. Am. Chem. Soc.* **130**, 13589–13597 (2008).
114. H. H. Hariri, A. M. Lehaf, J. B. Schlenoff, Mechanical properties of osmotically stressed polyelectrolyte complexes and multilayers: Water as a plasticizer. *Macromolecules* **45**, 9364–9372 (2012).
115. E. Yildirim, Y. Zhang, J. L. Lutkenhaus, M. Sammalkorpi, Thermal transitions in polyelectrolyte assemblies occur via a dehydration mechanism. *ACS Macro Lett.* **4**, 1017–1021 (2015).
116. Y. Zhang, F. Li, L. D. Valenzuela, M. Sammalkorpi, J. L. Lutkenhaus, Effect of water on the thermal transition observed in poly(allylamine hydrochloride)–poly(acrylic acid) complexes. *Macromolecules* **49**, 7563–7570 (2016).
117. R. Zhang, Y. Zhang, H. S. Antila, J. L. Lutkenhaus, M. Sammalkorpi, Role of salt and water in the plasticization of PDAC/PSS polyelectrolyte assemblies. *J. Phys. Chem. B* **121**, 322–333 (2017).
118. Y. Zhang *et al.*, Molecular origin of the glass transition in polyelectrolyte assemblies. *ACS Cent. Sci.* **4**, 638–644 (2018).
119. P. Batys, Y. Zhang, J. L. Lutkenhaus, M. Sammalkorpi, Hydration and temperature response of water mobility in poly(diallyldimethylammonium)-poly(sodium 4-styrenesulfonate) complexes. *Macromolecules* **51**, 8268–8277 (2018).
120. P. Batys, S. Kivistö, S. M. Lalwani, J. L. Lutkenhaus, M. Sammalkorpi, Comparing water-mediated hydrogen-bonding in different polyelectrolyte complexes. *Soft Matter* **15**, 7823–7831 (2019).
121. R. E. Bulo *et al.*, "Site binding" of Ca^{2+} ions to polyacrylates in water: A molecular dynamics study of coiling and aggregation. *Macromolecules* **40**, 3437–3442 (2007).
122. H. Dautzenberg, J. Kriz, Response of polyelectrolyte complexes to subsequent addition of salts with different cations. *Langmuir* **19**, 5204–5211 (2003).
123. S. Perry, Y. Li, D. Priftis, L. Leon, M. Tirrell, The effect of salt on the complex coacervation of vinyl polyelectrolytes. *Polymers (Basel)* **6**, 1756–1772 (2014).
124. D. Iyer, V. M. S. Syed, S. Srivastava, Influence of divalent ions on composition and viscoelasticity of polyelectrolyte complexes. *J. Polym. Sci* **59**, 2895–2904 (2021).
125. T. K. Lytle, C. E. Sing, Tuning chain interaction entropy in complex coacervation using polymer stiffness, architecture, and salt valency. *Mol. Syst. Des. Eng.* **3**, 183–196 (2018).
126. R. Triolo, J. R. Grigera, L. Blum, Simple electrolytes in the mean spherical approximation. *J. Phys. Chem.* **80**, 1858–1861 (1976).
127. J. Israelachvili, *Intermolecular and Surface Forces* (Academic Press, 2011).
128. E. Darve, D. Rodríguez-Gómez, A. Pohorille, Adaptive biasing force method for scalar and vector free energy calculations. *J. Chem. Phys.* **128**, 144120 (2008).
129. J. Comer *et al.*, The adaptive biasing force method: Everything you always wanted to know but were afraid to ask. *J. Phys. Chem. B* **119**, 1129–1151 (2015).
130. G. Fiorin, M. L. Klein, J. Hénin, Using collective variables to drive molecular dynamics simulations. *Mol. Phys.* **111**, 3345–3362 (2013).
131. M. Miao *et al.*, Avoiding non-equilibrium effects in adaptive biasing force calculations. *Mol. Simul.* **47**, 390–394 (2021).